



Cold collision and the determination of the $X^2\Sigma_{1/2}(v=1, N=1) \rightarrow A^2\Pi_{1/2}(v'=0, J'=1/2)$ frequency with buffer-gas-cooled MgF molecules

Supeng Xu^a, Meng Xia^a, Ruoxi Gu^a, Chunying Pei^a, Zhenghai Yang^a, Yong Xia^{a,b,*}, Jianping Yin^{a,**}

^aState Key Laboratory of Precision Spectroscopy, Department of Physics, East China Normal University, Shanghai 200062, China

^bNYU-ECNU Institute of Physics at NYU Shanghai, Shanghai 200062, China



ARTICLE INFO

Article history:

Received 15 June 2019

Revised 23 July 2019

Accepted 23 July 2019

Available online 24 July 2019

ABSTRACT

We report a detailed experimental study of the cold collision of magnesium mono-fluoride (MgF) with buffer gas and compare the cryogenic molecular beam source of two different inner structures of cell. The collision cross section with helium is measured to be $\sim 0.8 \times 10^{-14} \text{ cm}^2$ at 7.5 K, which is suitable for buffer-gas cooling. The absorption spectrum around 368.7 nm at low-lying rotational states is assigned and the accurate frequency of $X^2\Sigma_{1/2}(v=1, N=1) \rightarrow A^2\Pi_{1/2}(v'=0, J'=1/2)$ transition is determined to be 812.959246 THz, which is essential for constructing the quasi-closed cycling between vibrational states. Our study is an important complement to laser cooling of MgF molecules.

© 2019 Elsevier Ltd. All rights reserved.

1. Introduction

During the past three decades, studies of cold and ultra-cold atoms have been developed into a very mature field with tremendous achievements [1,2]. Now scientists are also eager to produce cold molecule samples, owing to their rich internal degrees of freedom, large electric dipole moments, unique chemical characteristics and so on, which atoms do not possess inherently. Cold molecules provide new possibilities for precision measurement [3,4], quantum information science [5,6], condensed-matter physics [7], and controlled chemistry [8]. Inspired by such fascinating applications, a variety of methods have been invented to create cold molecules. For instance, (ac) Stark decelerating [9,10] and Zeeman slowing [11] have been developed to slow down a molecular beam to be a few meters per second with \sim mK temperature. In the meanwhile, velocity filtering [12] and buffer gas cooling [13] have produced cold samples at tens of meters per second with \sim K temperature. Photo-association [14] and Feshbach resonance [15] techniques have also been successfully used to prepare ultracold molecular samples, but they are limited to molecules that can be created from laser-coolable atoms, thereby ruling out interesting species like fluorides, oxides, and poly-atomics. In addition, the

opto-electrical cooling techniques have also successfully been reported in cooling polyatomic molecules CH₃F and H₂CO to sub-mK temperature [16]. Direct laser cooling [17], which is believed to be able to bridge the “ μ K” gap, is a relatively new direction but has achieved great progress in recent years. Besides some polar molecules (SrF [18,19], CaF [20,21], YO [22], Ybf [23]) that have been demonstrated, there are many more candidate molecules that are appropriate for laser cooling, such as the ongoing BaF [24], BaH [25], BH [26] and even polyatomic molecule SrOH [27].

In our group, laser cooling of MgF molecule experiment is being conducted. MgF, as a candidate molecule, has highly diagonal Franck-Condon factors (FCFs), which means only two laser frequencies are enough to construct the quasi-cycling transition [28]. After a lot of attempts of direct laser ablation of compounds containing MgF, we find that it is more efficient to create MgF by chemical reaction of magnesium with gas containing fluoride [29]. This may be attributed to the metalloid character of Mg, since it is located in the second line of group II atoms. As far as we know, calcium mono-fluoride is also created by chemical reaction though calcium is a little more active than magnesium [30].

One problem we face is to optimize the cryogenic beam source, and find the optimum structures of cell suitable for MgF to create a high-flux beam, which will have great influence on our following experiment. Another concern is to determine the exact $X(v=1, N=1) \rightarrow A(v'=0, J'=1/2)$ frequency necessary for cooling molecules, which is a challenging task, since the population at

* Corresponding author at: State Key Laboratory of Precision Spectroscopy, Department of Physics, East China Normal University, Shanghai 200062, China.

** Corresponding author.

E-mail addresses: yxia@phy.ecnu.edu.cn (Y. Xia), jpyin@phy.ecnu.edu.cn (J. Yin).

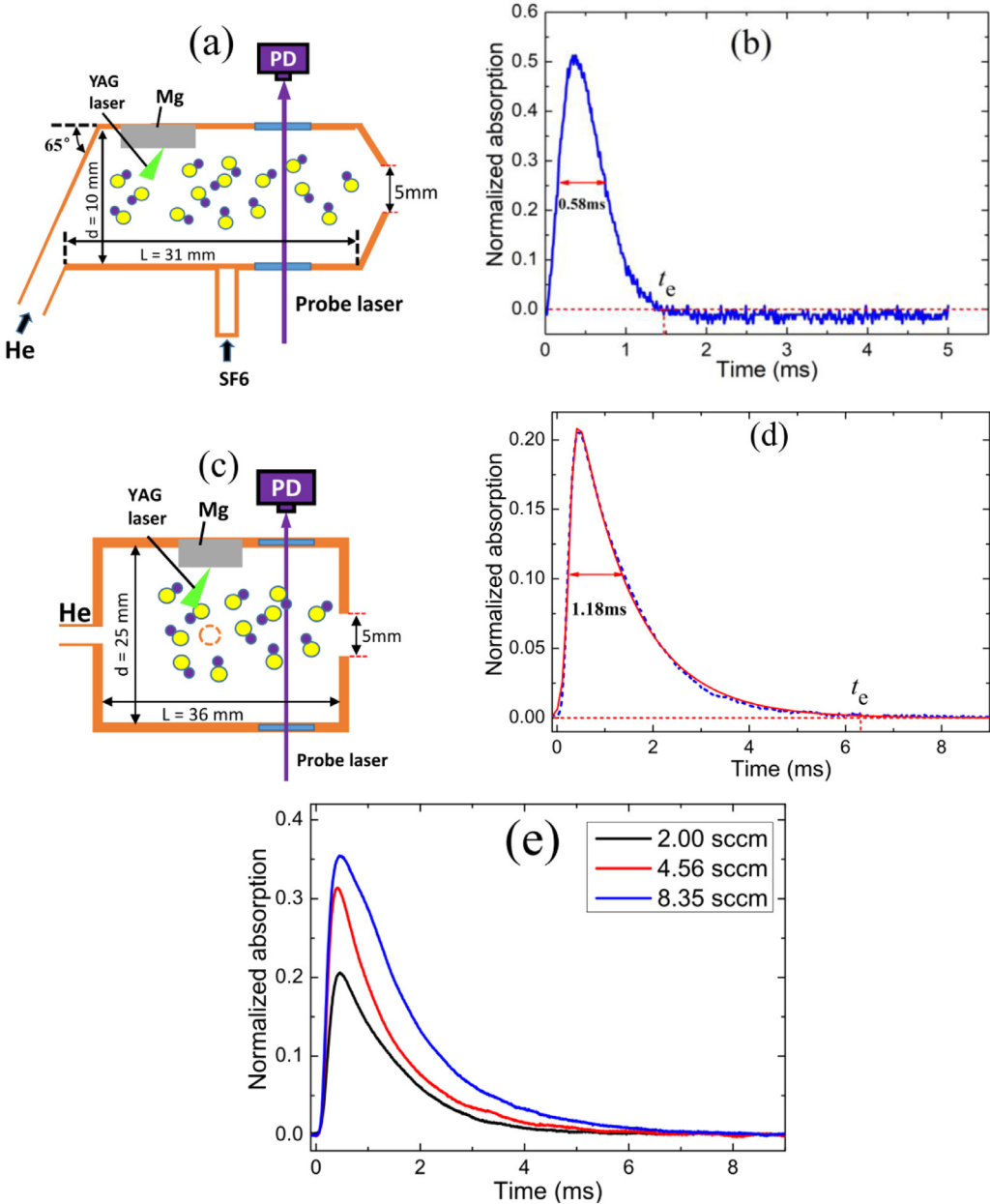


Fig. 1. (a) A simplified schematic of a buffer gas cell where helium is flowed into through an angled tube. The important physical dimensions (cell length, $L=31$ mm, cell diameter, $d=10$ mm, the aperture, 5 mm, and the bevel angle of the helium tube is 65°). A probe laser passing through the cell is used to observe molecular absorption. (b) Typical absorption signal of molecules from the beveled cell at 359.3 nm. (c) A simplified schematic of a buffer gas cell with the rectangular structure. The cell length, $L=36$ mm, cell diameter, $d=25$ mm, and the aperture, 5 mm. (d) The blue dashed line is the measured absorption signal of the rectangular cell at 359.3 nm, while the red solid line is a theoretical fit with Eq. (2), in which there is a long time of decay. (e) The absorption signal for three He flow rates with the rectangular cell, where the flow rate of SF_6 is fixed to 0.05 sccm.

$X^2\Sigma_{1/2}(v=1)$ state for 6 K is almost zero, thus lead to a very weak signal and there is almost no literature we can refer to.

In this paper, we demonstrate the effective creation of MgF molecules with chemical reaction for two various cell geometries, and compare their absorption curves to obtain the optimal condition for preparation of MgF, that is, a shorter pulse, higher efficiency of extraction, and a shorter time of extraction. The cold collision cross section between MgF and helium is measured. We theoretically calculated the spectra of the $X^2\Sigma_{1/2}(v=1)$ to $A^2\Pi(v'=0)$ transitions using the parameters from the fittings [29], and measured the weak absorption signal of transitions around 368.7 nm. By fitting the lines of the transitions near the neighborhood of the zero gap (the starting lines of the P, Q, and R branches), we find

that the experimental values are in excellent consistence with the theoretical results. Our measurement is of high precision and resolution with an uncertainty of 30 MHz from the wavemeter.

2. The comparison of two types of cryogenic cell

The details of our cryogenic apparatus can be referenced to Ref [29]. Here, we give a brief description. We used the reaction of laser-ablated Mg and gaseous SF_6 , which is heat-insulated by a polyimide spacer, to produce high-density MgF radicals. The created molecules are cooled and swept out of the cell by a flow of precooled helium gas. Two layers of copper shield attached to the cold plates are used to prevent room temperature radiation from

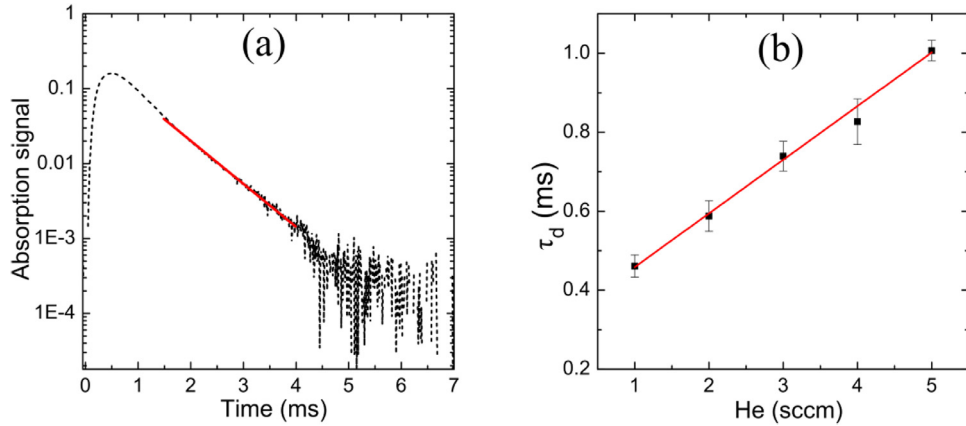


Fig. 2. (a) Absorption fraction decay curve with log scale. The red line is the exponential decay fitting, which can be used to measure the collision cross section of MgF with helium. (b) Decay time vs the flow rate, where the density of the helium is calculated by Eq. (5) at the diffusive limit. The data points can be well fitted linearly to get the slope and calculate the collision cross section.

impinging directly upon the cold cell, and a layer of activated charcoal is attached to the inner surface of the second radiation cylinder to absorb helium gas at 6 K. The power of the pulsed ablation laser (Nd: YAG, 10 ns duration, 532 nm, 2 Hz) used in experiment is 17 – 19 mJ and the temperature of the tube where SF₆ flows into is heated to 240 K to prevent the gas from freezing.

There are two sets of commercial Ti:sapphire lasers (Matisse TS) in our laboratory, both of which have a large tuning range of 700–1030 nm and high output power. In experiment, the cooling frequencies of MgF (pumping: 359.3 nm and repumping: 368.7 nm) are obtained by doubling the lasers, and are locked to a reference cavity [31].

We have two science cells with different structures, as shown in Fig. 1(a) and (c). One is identical to the design of Ref [30], and we called it “bevelled cell”, another one is made of a cubic copper with two cross holes [32]. In Fig. 1(a), helium gas enters into the cell through an angled tube and is directed towards the solid target, while in Fig. 1(c), the helium gas is flowed into from the rear of the cell. For the rectangular cell, the SF₆ is flowed into from the bottom, as shown by the dashed circles. For another cell, the reaction gas is poured into from the side of ablation light, which can be clearly seen in Ref [29]. During our experiment, the temperature of the rectangular cell can only be cooled to 7.5 K, since it has a larger load, while for the other, it can be cooled to 6 K. We introduced two various types of cell here, because we want to compare the characteristics of preparing MgF molecules of the two different structures, optimize the cryogenic molecular beam source, and measure the collision cross section with helium buffer gas using the rectangular cell. An absorption spectroscopy scheme is set up to detect and monitor the molecule creation and collision dynamics for both of the two kinds of cell. In order to extract the information behind the signal, we normalized it to the absorption fraction $c = 1 - I_{\text{abs}}/I_{\text{avg}}$, where I_{avg} is the mean value of the background signal. Fig. 1(b) shows a typical absorption signal of the bevelled cell with the depletion efficiency ~50% at 359.3 nm, which has a full width at half maximum (FWHM) of 0.58 ms. The absorption signal curve of the rectangular cell is shown in Fig. 1(d) in blue dashed line, where the depletion efficiency is ~20% and the FWHM is 1.18 ms, which is ~40% and ~2 times of that of bevelled cell, respectively. Compared with the rectangular structure, the total time necessary for the molecules to be extracted out of the cell for the bevelled structure, t_e , is much smaller, yielding a short pulse and leaving little time for diffusion to the walls. The flow rates for helium and SF₆ here are 2 and 0.05 sccm separately. A larger flow rate of helium for the rectangular cell results in a bigger absorption signal, but there is still an upper limit, which is illustrated

in Fig. 1(e). Besides, the extraction time increases with the higher flow of helium, especially for the blue solid line at a flow rate of 8.35 sccm, in which there is a significant broadening. We attribute this phenomenon to the growing vortices size with the increase of helium flow rate [33], which can not only trap a large fraction of molecules formed by chemical reaction but also diffuse them to the walls, thus limit the fraction that can be extracted out of the cell. Also, a large flow rate of continuous helium will limit the lifetime of the magneto-optical trapping of molecules [21,22], so a bevelled cell is adopted in our following experiment. However, to measure the diffusion collision cross section with buffer gas, we conduct an experiment using the rectangular cell in the next section [24,34], while the other parts of this paper were conducted using the bevelled cell.

3. Collisional cross section with buffer gas

We construct a two-step model to fit the absorption signal of the rectangular cell. First, the molecule's creation process is modeled by a logistic function,

$$y = \frac{A}{1 + e^{-(t-t_0)/\tau_1}}, \quad (1)$$

where t_0 means the delay after the pulse laser fired, and it depends on the distance between the target and the probe beam. τ_1 evaluates how fast the creation process happens.

The second step is the decay process caused by the diffusion of molecules in the buffer-gas cell, including the colliding with the cell walls and inelastic collisions with the buffer gas. Overall, we can model it with an exponential decay, so the two-step model gives a fitting function,

$$y = \frac{A}{1 + e^{-(t-t_0)/\tau_1}} e^{-(t-t_0)/\tau_2}, \quad (2)$$

where τ_2 describes how fast the signal decay. This two-step model fits well with the experimental data as shown in red solid line in Fig. 1(d). Once the molecules are created by the ablation laser, the signal decays. The relaxations are mainly caused by the diffusion to the cell walls and the leakage via the aperture to form a molecular beam. Fig. 2(a) illustrates the absorption signal on a logarithmic scale, in which the helium flow rate is 5 sccm. From 1.5 to 4 ms, the logarithmic signal can be fitted well with a line, which reflects the in-cell colliding dynamics. The time constant of the exponential decay for molecules diffusing through the helium gas of density (n_{He}) is given by [34],

$$\tau_d = \frac{n_{\text{He}}\sigma_d}{\bar{v}G}, \quad (3)$$

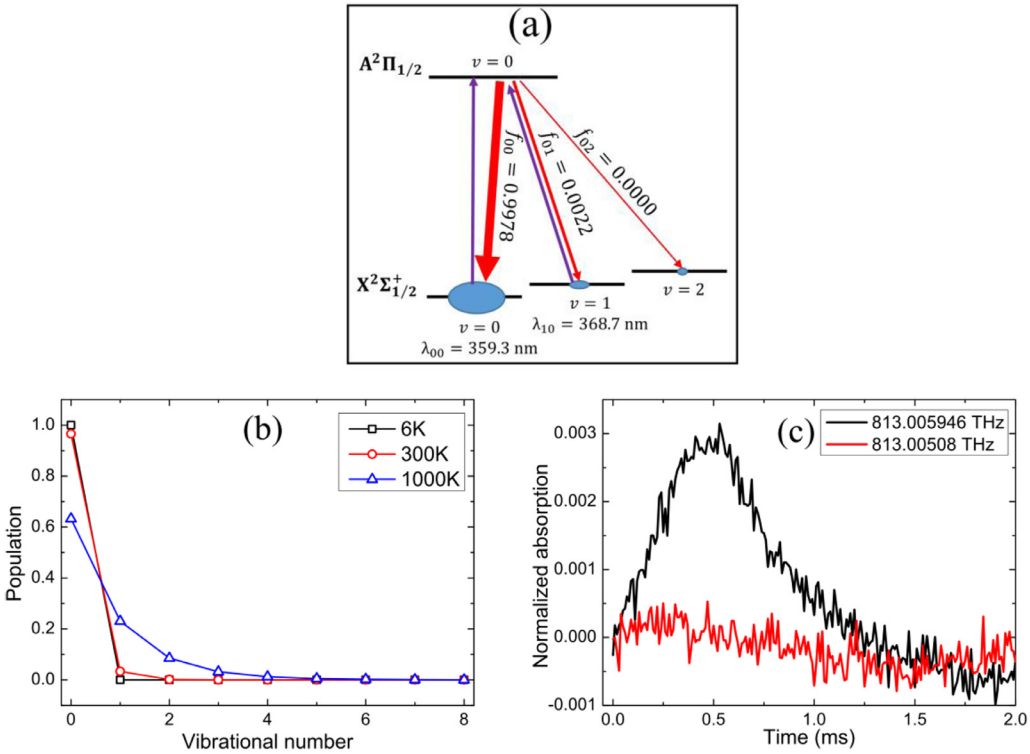


Fig. 3. (a) Relevant electronic and vibrational structure in MgF. Solid upward lines indicate laser-driven transitions at the wavelength λ_{vv} . Solid downward lines indicate the spontaneous decays from the $A^2\Pi_{1/2}$ state with FCFs f_{vv} as shown. The blue ellipses represent the population of molecules at each vibrational state. (b) Theoretical calculation of the vibrational distribution. The population at high-lying vibrational states are very small till the temperature is up to 1000 K. At 6 K, almost all the molecules populate at the $v=0$ state. (c) The absorption signal at 813.005946 THz, which is the $Q_1(1)$ branch of $v=1 \rightarrow v'=0$ transitions. The red curve is from an irrelevant frequency, which is plotted here for comparison.

$$G = \frac{3\pi}{32} \left(\frac{j_{01}^2}{r^2} + \frac{\pi^2}{L^2} \right), \quad (4)$$

where σ_d is the collision cross section between molecule and the buffer gas, $\bar{v} = (8k_B T / \pi \mu)^{1/2}$ is the average MgF-⁴He collision velocity at temperature T , μ is the reduced mass of atom-molecule system, r and L are the radius and length of the cylindrical tube, respectively, and $j_{01} \approx 2.405$ is the first root of the Bessel function $J_0(x)$ [34].

The density of helium is determined by [35],

$$n_{\text{He}} = \frac{\kappa f}{A\beta}, \quad (5)$$

where A is the area of the aperture, $\beta \equiv \sqrt{2k_B T / m_{\text{He}}}$, $\kappa = 2\sqrt{\pi}$ for fully effusive and $\kappa = 1/\sqrt{\gamma/(\gamma - 1)}$ (for a noble gas the heat capacity is $\gamma = 5/3$) for fully supersonic. In our case at the low helium flow rate regime (in the effusive regime), 1 sccm corresponds to the He density of about $4.58 \times 10^{14} \text{ cm}^{-3}$.

Fig. 2(b) shows the dependence of the decay time constant τ_d on the helium flow rate, along with a linear fitting. Using the Eq. (3), we find that the diffusion cross section in He at 7.5 K to be $\sim 0.8 \times 10^{-14} \text{ cm}^2$, which is consistent with the typical helium-molecule elastic cross section of $\sim 10^{-14} \text{ cm}^2$ [36].

4. The determination of the v_{01} frequency

In order to achieve laser cooling of MgF molecules, one need to construct the quasi-cycling system between the $X^2\Sigma^+ \rightarrow A^2\Pi_{1/2}$ transition. That means at least two laser frequencies are necessary for MgF, since it has supportive FCFs [28]. A molecule can scatter $\sim 10^6$ photons before it is populated at a dark state with only

two lasers [31]. The recoil velocity for MgF is $\hbar k/m \sim 2.6 \text{ cm/s}$, so in principle that's enough to slow down the molecular beam with the longitudinal velocity of 200 m/s for our laser cooling experiment. According to the Maxwell-Boltzmann distribution law, the number of molecules in each of the vibrational states is proportional to $e^{-E/kT}$, where k is the Boltzmann's constant, T is the absolute temperature and E is the discrete vibrational energy [37]:

$$E = hc \times (G(0) + G_0(v)), \quad (6a)$$

$$G(0) = \frac{1}{2}w_e - \frac{1}{4}w_e x_e + \frac{1}{8}w_e y_e + \dots, \quad (6b)$$

$$G_0(v) = w_0 v - w_0 x_0 v^2 + w_0 y_0 v^3 + \dots, \quad (6c)$$

$$w_0 = w_e - w_e x_e + \frac{3}{4}w_e y_e + \dots, \quad (6d)$$

$$w_0 x_0 = w_e x_e - \frac{3}{2}w_e y_e + \dots, \quad (6e)$$

$$w_0 y_0 = w_e y_e + \dots, \quad (6f)$$

where $G(0)$ is the zero-point energy, $G_0(v)$ is the energy of each vibrational states with reference to $G(0)$, and w_e , $w_e x_e$, and $w_e y_e$ are the harmonic vibrational constant, and the first and second anharmonic corrections to the harmonic oscillator, respectively. The zero-point energy can be left out since to add this to the exponent would mean only adding a factor that is constant for all the vibrational levels (including the zero level). Table 1 lists some of the parameters used in our calculation.

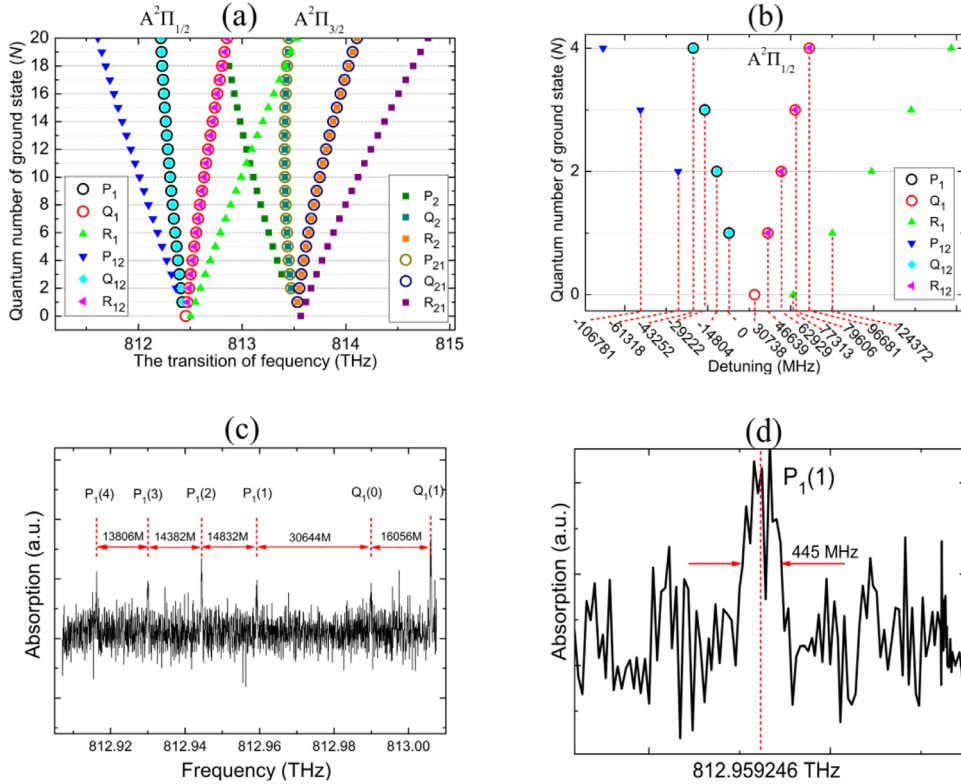


Fig. 4. (a) The calculated bands of the $X^2\Sigma_{1/2}(v=1) \rightarrow A^2\Pi(v'=0)$ system with the constants listed in Table 2. (b) The bands of the $X^2\Sigma_{1/2}(v=1) \rightarrow A^2\Pi_{1/2}(v'=0)$ transitions in the low-lying rotational states, where the zero point is set at $P_1(1)$ branch. (c) The measured spectra in the cryogenic cell near the 368.7 nm. (d) The measured $P_1(1)$ branch of $v=1 \rightarrow v'=0$ transitions, and the accurate frequency is 812.959246 THz. The data in figure (c) and (d) are from the absorption signals of MgF molecules in the cell.

Table 1
Spectroscopic constants for the $X^2\Sigma^+$ electronic states of MgF from the experimental data.

State	w_e (cm ⁻¹)	wex_e (cm ⁻¹)	wey_e (cm ⁻¹)
$X^2\Sigma^+$	720.14 [38]	4.26 [38]	0.0165 [38]

However, using the Eq. (6), we find that the population at the first vibrational state ($v=1$) of $X^2\Sigma^+$ electronic state for 6 K is almost zero, shown in Fig. 3(b). Even at a room temperature, the population at $v=1$ state is much smaller than that at $v=0$ state. What's more, once a molecule absorbs a photon from the probe laser, 99.78% probability it will go back to the $X^2\Sigma^+(v=0)$ state [28], as can be seen in Fig. 3(a), which makes the molecules populate at $v=1$ state even much less, and thus increase the difficulties of measuring the spectrum around 368.7 nm, because the fluctuations of the background can even bigger than the real signal. Fig. 3(c) is a normalized absorption curve at 813.005946 THz (368.7 nm), with an average of 120 times. The absolute absorption fraction is ~ 0.003 , which is $\sim 1/167$ of that absorption fraction from 359.3 nm. We also plot a curve at an irrelevant frequency (813.005080 THz) for reference.

As far as we can tell, there is a striking feature for the vibration-rotation spectra of MgF in the neighborhood of the zero gap. The spacing between the $P_1(1)$ and the $Q_1(0)$ associated with the $X^2\Sigma_{1/2} \rightarrow A^2\Pi_{1/2}$ transitions is quite large, which is an effective way to assign the lines. Using the formulas in Ref [29], we calculated the spectra of the $X^2\Sigma_{1/2}(v=1)$ to $A^2\Pi_{1/2}(v'=0)$ transitions, as shown in Fig. 4(a). In the figures, the y axis is the rotational quantum numbers of the ground state, N , and the x axis is the transition frequency. The spectrum constants used here are listed in Table 2, including the rotational constant of the

$A^2\Pi$ state B'_v , the rotational constant of the $X^2\Sigma$ state B_v , the spin-orbit coupling constant A , the spin-rotational coupling constant γ , and the zero lines v'_0 and v_0 for $A^2\Pi$ and $X^2\Sigma_{1/2}(v=1)$, respectively.

From the figure, the transitions of $X^2\Sigma_{1/2}(v=1) \rightarrow A^2\Pi_{1/2}(v'=0)$ are located near 812.5 THz, while the transitions of the $X^2\Sigma_{1/2}(v=1) \rightarrow A^2\Pi_{3/2}(v'=0)$ are near 813.5 THz. Fig. 4(b) is the partial enlarged figure of the $X^2\Sigma_{1/2}(v=1) \rightarrow A^2\Pi_{1/2}(v'=0)$ transitions near the zero gap, in which the x axis is represented by frequency detuning with respect to $P_1(1)$. We can see that the frequency difference between $P_1(1)$ and $Q_1(0)$ is 30,738 MHz, which is almost twice of the other sequences in P_1 and Q_1 branches. The first three sequences in P_1 branch are 14,804, 14,418, and 14,030 MHz and the frequency difference between $Q_1(0)$ and $Q_1(1)$ is 15,901 MHz. Fig. 4(c) shows the measured absorption bands of MgF near 368.7 nm. Though it is weak, we still can figure out some peaks. A key step to confirm the peak is real or not is to see whether the peak is made up of a series continuous data points, since the fluctuations from noise are random. The frequency differences between the measured peaks are labeled in the Fig. 4(c), along with the assignment of the peaks, which are in excellent consistence with the calculated results. Taking the $P_1(1)$ line in Fig. 4(d), its peak width is 445 MHz due to the Doppler broadening ($\Delta\nu_D = 2v_0\sqrt{\frac{2kT\ln 2}{mc^2}} = 223$ MHz) of MgF at 6 K.

The exact frequency values in Fig. 4(c) are listed in Table 3, where N represents the rotational quantum number of the ground state, and O – C represents the frequency difference between the observed and calculated lines. From the table, the measured values are away from the calculated ones by about 0.533 THz, which may because that the constants used in our calculation are partly from the fitting of the high-lying rotational states.

Table 2The constants for calculating the spectra bands of $X^2\Sigma_{1/2}(v=1) \rightarrow A^2\Pi(v'=0)$.

B'_v (cm $^{-1}$)	B_v (cm $^{-1}$)	A (cm $^{-1}$)	v'_0 (cm $^{-1}$)	v_0 (cm $^{-1}$)	γ (cm $^{-1}$)
0.5264 [29]	0.51217 [39]	36.406 [29]	27,830.0 [29]	711.69 [39]	0.0016595 [40]

Table 3Measured and calculated frequencies for the transition $X^2\Sigma_{1/2}(v=1) \rightarrow A^2\Pi_{1/2}(v'=0)$. The column on the right summarizes the energy difference between the observed and calculated lines.

N	Cal. (THz)	Obs. (THz)	O – C
P ₁	812.425816	812.959246	0.533430
	812.411012	812.944414	0.533402
	812.396594	812.930032	0.533438
	812.382564	812.916226	0.533662
Q ₁	812.456550	812.989890	0.533340
	812.472455	813.005946	0.533491

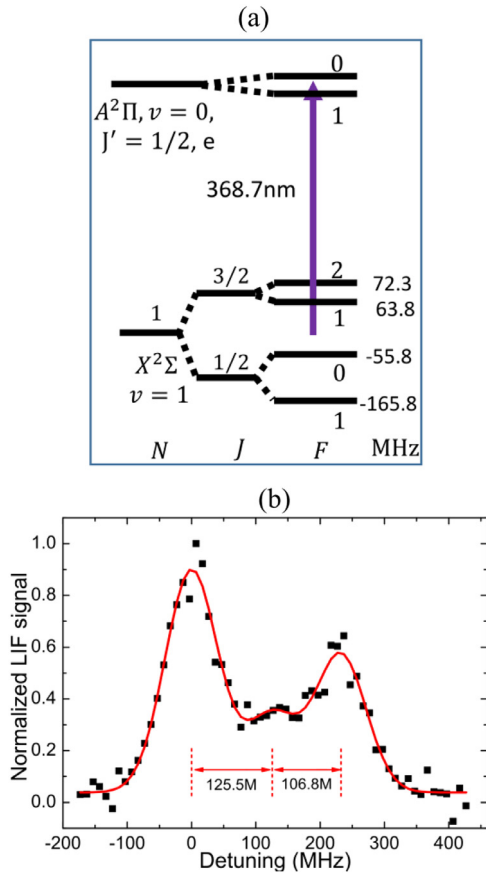
**Fig. 5.** (a) Hyperfine-structure levels of the $X^2\Sigma_{1/2}(v=1, N=1)$ to $A^2\Pi_{1/2}(v'=0, J'=1/2, e)$ transition of MgF molecule. The hyperfine levels for $N=1$ are shown. (b) LIF spectra of the transition from $X^2\Sigma_{1/2}(v=1, N=1)$ to $A^2\Pi_{1/2}(v'=0, J'=1/2, e)$. The red curve is a Gaussian fitting.

Fig. 5(a) shows the energy levels of $X^2\Sigma_{1/2}(v=1, N=1) \rightarrow A^2\Pi_{1/2}(v'=0, J'=1/2)$ transition, which corresponding to the P₁(1) branch in **Fig. 4(c)**. The hyperfine splitting of the $X^2\Sigma_{1/2}$ with $J=1/2$ is ~ 110 MHz, while the splitting between the $F=0$ ($J=1/2$) and the $F=1$ ($J=3/2$) levels is ~ 120 MHz. The splitting of $J=3/2$ is ~ 8.5 MHz, which is within the spontaneous emission rate and cannot be resolved in our experiment. The hyperfine splitting within the excited $A^2\Pi_{1/2}$ state is only a few MHz, which is not resolvable.

Fig. 5(b) shows the measured laser induced fluorescence (LIF) of the molecules with $X^2\Sigma_{1/2}(v=1, N=1) \rightarrow A^2\Pi_{1/2}(v'=0, J'=1/2)$ transition. We obtain a hyperfine splitting of ~ 125.5 and ~ 106.8 MHz, which are consistent with the theoretical values in **Fig. 5(a)**. The discrepancies are mainly from the weak LIF signal of $v=1 \rightarrow v'=0$ transition.

5. Conclusion

To conclude, we compare the characteristics of two various structures of cell in preparing the cryogenic molecular beam source of MgF. Using the rectangular cell, the collision cross section between MgF and helium is measured. The partial P and Q branches of electronic transition of $X^2\Sigma_{1/2}(v=0, N=1) \rightarrow A^2\Pi_{1/2}(v'=0, J'=1/2)$ are also measured and confidently assigned. Finally, we introduced an effective way to assign the spectra of unknown, which can be applied to other molecules suitable for laser cooling.

Acknowledgments

We acknowledge the financial support from the [National Natural Science Foundation of China](#) under grants 11834003, 91836103, 91536218, 11374100, [Natural Science Foundation of Shanghai Municipality](#) under grant 17ZR1443000, Joint Research Institute for Science and Society (JoRISS), and the 111 project of China under Grant No. B12024.

References

- [1] Chu S. Rev Mod Phys 1998;70:685.
- [2] Ketterle W. Rev Mod Phys 2002;74:1131.
- [3] Baron J, Campbell WC, DeMille D, Doyle JM, Gabrielse G, Gurevich YV, Hess PW, Hutzler NR, Kirilov E, Kozyryev I, O'Leary BR, Panda CD, Parsons MF, Petrik ES, Spaun B, Vutha AC, West AD. Science 2014;343:269.
- [4] Hudson JJ, Kara DM, Smallman IJ, Sauer BE, Tarbutt MR, Hinds EA. Nature 2011;473:493.
- [5] DeMille D. Phys Rev Lett 2002;88:067901.
- [6] André A, DeMille D, Doyle JM, Lukin MD, Maxwell SE, Rabl P, Schoelkopf RJ, Zoller P. Nat Phys 2006;2:636.
- [7] Micheli A, Brennen GK, Zoller P. Nat Phys 2006;2:341.
- [8] Krems RV. Phys Chem Chem Phys 2008;10:4079.
- [9] Hudson ER, Lewandowski HJ, Sawyer BC, Ye J. Phys Rev Lett 2006;96:143004.
- [10] Bishop AI, Wang L, Barker PF. New J Phys 2010;12:073028.
- [11] Narevicius E, Libson A, Parthey CG, Chavez I, Narevicius J, Even U, Raizen MG. Phys Rev A 2008;77:051401.
- [12] Rangwala SA, Junglen T, Rieger T, Pinkse PWH, Rempe G. Phys Rev A 2003;67:043406.
- [13] Weinstein JD, deCarvalho R, Guillet T, Friedrich B, Doyle JM. Nature 1998;395:148.
- [14] Sage JM, Sainis S, Bergeman T, DeMille D. Phys Rev Lett 2005;94:203001.
- [15] Ni KK, Ospelkaus S, de Miranda MHG, Péter A, Neyenhuis B, Zirbel JJ, Kotchigova S, Julienne PS, Jin DS, Ye J. Science 2008;322:231.
- [16] Prehn I, Ibrügger M, Glöckner R, Rempe G, Zeppenfeld M. Phys Rev Lett 2016;116:063005.
- [17] Carr LD, DeMille D, Krems RV, Ye J. New J Phys 2009;11:055049.
- [18] Shuman ES, Barry JF, Demille D. Nature 2010;467:820.
- [19] Norrgard EB, McCarron DJ, Steinecker MH, Tarbutt MR, DeMille D. Phys Rev Lett 2016;116:063004.
- [20] Truppe S, Williams HJ, Hambach M, Caldwell L, Fitch NJ, Hinds EA, Sauer BE, Tarbutt MR. Nat Phys 2017;13:1173.
- [21] Anderegg L, Augenbraun BL, Chae E, Hemmerling B, Hutzler NR, Ravi A, Collopy A, Ye J, Ketterle W, Doyle JM. Phys Rev Lett 2017;119:103201.
- [22] Collopy AL, Ding S, Wu Y, Finnegan IA, Anderegg L, Augenbraun BL, Doyle JM, Ye J. Phys Rev Lett 2018;121:213201.
- [23] Lim J, Almond JR, Trigatzi MA, Devlin JA, Fitch NJ, Sauer BE, Tarbutt MR, Hinds EA. Phys Rev Lett 2018;120:123201.
- [24] Bu W, Chen T, Lv G, Yan B. Phys Rev A 2017;95:032701.
- [25] Iwata GZ, McNally RL, Zelevinsky T. Phys Rev A 2017;96:022509.

- [26] Hendricks RJ, Holland DA, Truppe S, Sauer BE, Tarbutt MR. *Front Phys* 2014;2:51.
- [27] Kozryev I, Baum L, Matsuda K, Augenbraun BL, Anderegg L, Sedlack AP, Doyle JM. *Phys Rev Lett* 2017;118:173201.
- [28] Xu L, Yin Y, Wei B, Xia Y, Yin J. *Phys Rev A* 2016;93:013408.
- [29] Xu S, Xia M, Yin Y, Gu R, Xia Y, Yin J. *J Chem Phys* 2019;150:084302.
- [30] Truppe S, Hambach M, Skoff SM, Bulleid NE, Bumby JS, Hendricks RJ, Hinds EA, Sauer BE, Tarbutt MR. *J Mod Optic* 2017;65:246.
- [31] Yin Y, Xia Y, Li X, Yang X, Xu S, Yin J. *Appl Phys E* 2015;8:092701.
- [32] Li X, Xu L, Yin Y, Xu S, Xia Y, Yin J. *Phys Rev A* 2016;93:063407.
- [33] Bulleid NE, Skoff SM, Hendricks RJ, Sauer BE, Hinds EA, Tarbutt MR. *Phys Chem Chem Phys* 2013;15:12299.
- [34] Kozryev I, Baum L, Matsuda K, Olson P, Hemmerling B, Doyle JM. *New J Phys* 2015;17:045003.
- [35] Barry JF, Shuman ES, DeMille D. *Chem Chem Phys* 2011;13:18936.
- [36] Hutzler NR, Lu HI, Doyle JM. *Chem Rev* 2012;112:4803.
- [37] Herzberg G. Molecular spectra and molecular structure spectra of diatomic molecules, 1. 2nd ed. New York: D. Van Nostrand Reinhold Inc.; 1950.
- [38] Barber BE, Zhang KQ, Guo B, Bernath PF. *J Mol Spectrosc* 1995;169:583.
- [39] Barrow RF, Beale JR. *Proc Phys Soc* 1967;91:483.
- [40] Anderson MA, Allen MD, Ziurys LM. *Astrophys J* 1994;425(1 Part 2).